Antipolar 2D Metallicity with Tunable Valence Wx+ (5 ≤ x ≤ 5.6) in the Layered Monophosphate Tungsten Bronzes [Ba(PO4)2]WmO3m−3

Hicham Nimoh, Angel Arévalo-López, Quintin Meier, Claire Minaud, Marielle Huvé, Frédéric Capet, Andrés Cano, Robert Glaum, Olivier Mentré

Anti-polar 2D-metallicity with tuneable valence W^{x+} ($5 \leq x \leq 5.6$) in the layered monophosphate tungsten bronzes $[Ba(PO_4)_2]W_mO_{3m-3}$

Hicham Nimoh[1,2], Angel M. Arévalo-López[1], Quintin N. Meier[3], Claire Minaud[4], Marielle Huvé[1], Frédéric Capet[1], Andrés Cano[3], Robert Glaum[2,*], Olivier Mentré[1,*]

[1]UCCS (Unité de Catalyse et Chimie du Solide), Université de Lille, Centrale Lille/ENSCL,59000, Lille, France
[2]Institut für Anorganische Chemie, Rheinische Friedrich-Wilhelms Universität Bonn, Gerhard-Domagk-Str. 1, 53121 Bonn, Germany
[3]Institut NEEL CNRS/UGA UPR2940, 25 rue des Martyrs, BP 166, 38042, Grenoble, France
[4]Chevreul Institute: Univ. Lille, CNRS, INRAE, Centrale Lille, Univ. Artois, FR 2638 IMEC - Institut Michel-Eugène Chevreul, F-59000 Lille, France

*Email: olivier.mentre@univ-lille.fr and rglaum@uni-bonn.de

ABSTRACT: The newly discovered series of layered monophosphate tungsten bronzes (L-MPTB) $[Ba(PO_4)_2]W_mO_{3m-3}$ consist of *m*-layer-thick slabs of (A-site-empty perovskite) WO_6 octaedra separated by barium phosphate spacers. These compounds display a distinct 2D metallic behavior confined in the central part of the perovskite slabs. Here, we report the missing $m = 2$ member of this series, in which we observe a rather uncommon oxidation state 5+ of the tungsten atom. We have analyzed the structure-property relationships of this new compound in relation to the other members of the L-MPTB family. In particular, we have determined its crystal structure by means of single-crystal X-ray and electron diffraction and investigated its physical properties from resistivity, Seebeck-coefficient and heat-capacity measurements combined with first-principles calculations. All the L-MPTB compounds show metallic behavior down to 1.8 K without any clear charge-density-wave (CDW) order. The $m = 2$ member, however, displays an increased influence of the phosphate spacer that translates into anisotropic negative thermal expansion, reversed thermopower and reversed crystal-field splitting of the tungsten t_{2g} orbital. Furthermore, our analysis of the full $[Ba(PO_4)_2]W_mO_{3m-3}$ series reveals a systematic and significant W off-centering in their octahedral coordination. We identify the resulting anti-polar character of these W displacements as the crucial aspect behind the 2D metallicity of these systems: It leads to the presence of bound charges whose screening determines the distribution of mobile charges, which then tend to accumulate at the center of the $[W_mO_{3-m}]$ block. We argue that this mechanism is analogous to enhanced conductivity observed for charged domain walls in ferroelectrics, thus providing a general design rule to promote 2D metallicity in layered oxides and related systems.

INTRODUCTION

The so-called oxide bronzes [1] form an important class of materials due to their fundamental properties and applications. These include low-dimensional metallicity, charge-density-wave phenomena and superconductivity, as well as electrochromic properties useful in for instance smart windows. [2,3] The main building block of these systems are MO_6 octahedra as in the original sodium-doped tungsten oxide Na_xWO_3 [4], with M = Re, W, Ta, Mo, Nb, Mn, V, and Ti. [1] The different arrangements of these octahedra result in a large number of structural variants. Among these variants, the newly discovered series of layered monophosphate tungsten bronzes (L-MPTB) $[Ba(PO_4)_2]W_mO_{3m-3}$ emerges as a particularly intriguing set of materials. [5] The recent discovery of these compounds at $m = 3$, 4 and 5 has unveiled the existence a broad subclass of bronzes with general formula $[A(XO_4)_2]M_mO_{3m-3}$ and crystal structures as illustrated in Fig. 1

. Interestingly, the crystal and electronic structure of the L-MPTBs is exceptionally stable despite the presence of hidden-Fermi-surface-nesting features that result in charge-density-wave (CDW) instabilities in other/previous W bronzes. Indeed, the structurally related (or parent hereafter) MPTB's with mixed valent tungsten (V, VI) are generally considered as nearly-2D metals, where (in)commensurate W-displacements characterizing the CDW take place in covalent 3D-WO_3 sub-units, and are allowed due to relatively low crystal symmetry. [6,7] In contrast, in the trigonal L-MPTB series the thick and rigid $[Ba(PO_4)_2]^{4-}$ spacer layers enforce trigonal structures, preserved down to 1.8K, which hampers any clear development of 2D metal-instability. [5] This suggests additional factors influencing the structure-property relationships within this class of materials.

In this work, we extend the L-MPTB series to the novel *m* = 2 member, $[Ba(PO_4)_2]W_2O_3$, whose nominal tungsten valence ideally corresponds to the rather uncommon W^{5+} state. Note that in the parent $W^{5+}PO_5$ bronze the localized *vs.* itinerant electronic behavior is still controversial. [8,9] We find that $Ba(PO_4)_2W_2O_3$ displays 2D metallicity incrementally related to the W atoms at the centers of the *m*-thick, A-site vacant perovskite blocks. We show that, in addition to an inductive effect [10] between the insulating spacer and the WO_3 block, the crucial ingredient for the strict 2D-behavior, is the presence of anti-polar displacements within the WO_3 layers. The latter establishes an analogy with charged domain walls in ferroelectrics. In addition, for the new *m* = 2 compound, we argue that the vicinity of all W-atoms with the phosphate groups of the spacer has an increased importance, distinctive for specific anisotropic negative thermal expansion, reversed thermopower and reversal of the t_{2g} orbitals with the WO_6 polyhedra crystal-field splitting from *m* = 2 to *m* = 5. This results in a general picture of their structure-property relations that connects with other oxides.

RESULTS

Synthesis. The synthesis of the new *m* = 2 member of the L-MPTB series was achieved by adapting the solid-state reaction procedure described in [5]. This procedure consists of two steps. First, $BaCO_3$, $(NH_4)_2HPO_4$ and WO_3 were reacted in the ratio 1:1:(*m*–1/3) at 873 K in air. This reaction product is then reduced at 1273 K by freshly reduced W metal (1/3). This well established with stoichiometric ratio of the reactants route, however, failed to yield the targeted *m* = 2 compound, resulting in different mixtures in which the *m* = 3 member of the L-MPTB series predominates instead. This problem was overcome by producing in two-step reaction the targeted $Ba(PO_4)_2W_2O_3$ phase with a slight concentration of oxygen vacancies. This procedure allows the preparation of single phase material, which is in particular free of other L-MPTB phases with higher *m (see Fig. S1 for XRPD diffractogram* in the supporting Information for details*)*. However, we consider the ideal $Ba(PO_4)_2W^{5+}{}_2O_3$ crystal structure in our ab-initio calculations. Indeed, the stability of the fully stoichiometric phase was confirmed by single crystal XRD from grown crystal at the external surface of a pellet, as discussed below. The influence of the slight oxygen deficiency checked by neutron powder diffraction (NPD, see below) is out of the scope of this paper and will be detailed elsewhere.

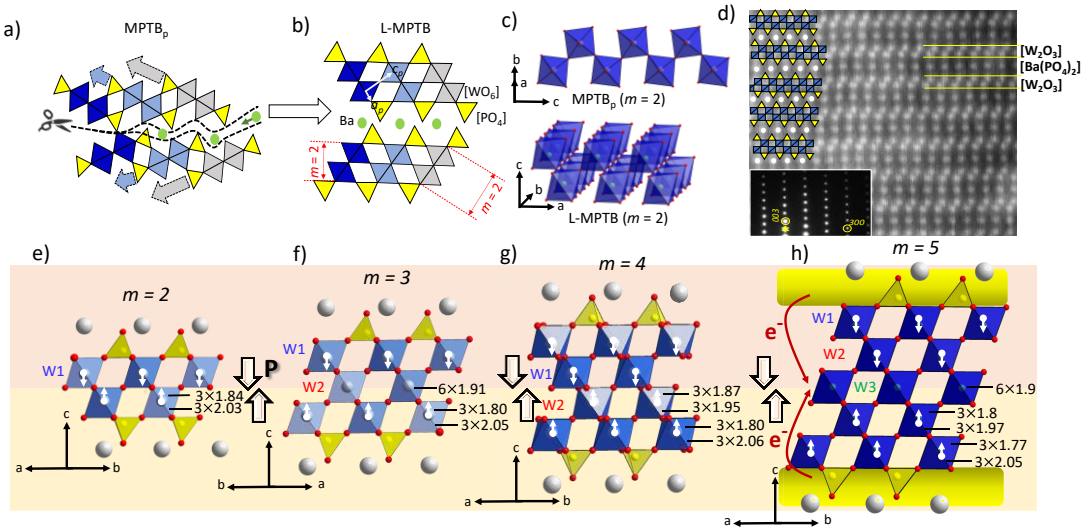

***Figure 1**. Sketch of the structural shift from MPTB$_p$ (a) to L-MPTB (b). The 1D W^{5+} chains displayed in $WOPO_4$ (MPTB$_p$ m = 2) vs. 2D-W^{5+} layers with double-octahedra in $Ba(PO_4)_2W_2O_3$ (L-MPTB m = 2) (c). HAADF images. The white spots correspond to the heavy Ba and W atoms, while the lighter P and O atoms are in the dark areas.*

The inset shows [010] ED patterns for the L-MPTB m = 2 (d). L-MPTB structure showing WO_6 octahedra with off-centering of W atoms, leading to anti-polar WO_3 blocks in m = 2 (e), m = 3 (f), m = 4 (g), m = 5 (h) analogous to charged domain walls in ferroelectric materials. The electron-donation from the P containing spacers to the walls is sketched in (h).

Crystal Structure. Starting from the well-known family of MPTB compounds, the structural shift to the L-MPTB is sketched in Fig. 1a,b for the *m* = 2 case by shearing of the chains into 2D units, and concomitant slicing of the 3D structure by insertion of the Ba^{2+} cations between the phosphate groups. Therefore, the *m* = 2 case peculiar leading either to *i)* 1D zigzag chains of $W^{5+}O_6$ octahedra in the *m* = 2 $WOPO_4$ parent bronzes, or to *ii)* double-octahedral perovskite layers in the *m* = 2 $Ba(PO_4)_2]W_2O_3$ L-MPTB, (see Fig. 1c). The later crystallizes in the trigonal space group *R*-3*m* (*a* = 5.2308(2) Å and *c* = 29.0237(11) Å at room temperature, R_F =1.90% from single crystal XRD data), see Table S1-3 in the supporting Information for details. Considering our specific synthesis method, we checked that the refinement of the single free O1 site (*i.e.* not part of a PO_4 group) occupancy converged to 1.00(4), although our polycrystalline sample may have some degree of oxygen deficiency. The Rietveld refinement of a polycrystalline sample using NPD data collected at room temperature (Institut Laue Langevin, D2b diffractometer, λ = 1.59Å, R_{Bragg} = 3.28%) is shown on the Fig. 2. After several tests, only the refinement of the O1 site occupancy at the center of the perovskite slabs, led to a slight deviation from the ideal stoichiometry leading to the $Ba(PO_4)_2W_2O_{2.92(5)}$ formula.

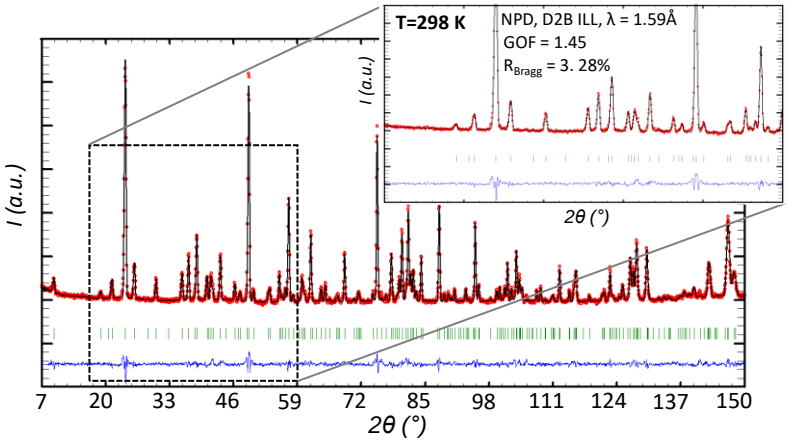

***Figure 2**. Experimental (red), calculated (black) and difference patterns after Rietveld refinement of NPD data for $Ba(PO_4)_2W_2O_{2.92(5)}$.*

Finally, the crystal structure $[Ba(PO_4)_2]W_2O_3$ obeys the structural principles established for the members at $2 \leq m \leq 5$, where the *m* index corresponds both to the number of stacked octahedra along both the trigonal *c*-axis and the pseudo perovskite-axis c_p. For *m* = 2, the aforementioned double perovskite layers of WO_6 octahedra are in between the $[Ba(PO_4)_2]^{2-}$ spacers, as sketched in Fig. 1b. In this figure the pseudo-cubic perovskite (a_p, c_p) axes are also highlighted. The W-W distance of 3.69 Å

(via a bridging oxygen atom) and the W-O-W angle of 180° mediate the electronic transport. The corresponding W-W distances along the L-MPTB series are given in Table S4 (see the supporting Information). Fig. 1d shows a high-angle annular dark-field (HAADF) image of structure for *m* = 2 projected on the (101) plane. As we see, the obtained intergrowth of the WO_3 blocks between the phosphate spacers is regular with no defects nor diffuse scattering lines. Further, we find that the crystal structure of the new *m* = 2 compound remains trigonal in the measured temperature range 19 K $\leq$ T $\leq$ 300 K, as is observed for other members of the L-MPTB series.

However, a slight elongation of the WO_6 octahedra occurs along the c-axis together with the off-centering of the W atoms as is illustrated in Fig. 1e for *m* = 2. It arises from anti-parallel displacements of these atoms along the c-axis, *i.e.* perpendicular and away from the barium-phosphate spacers. As a result, the WO_6 octahedra display long and short W-O bonds with distances 3 x 2.031(4) Å and 3 x 1.8459(2) Å for *m* = 2. This type of anti-polar displacements is characteristic of the full L-MPTB series as illustrated in Figs. 1 e-h and summarized in Table S4, in the supporting Information (see also [5]). Besides pseudo Jahn-teller considerations, whose amplitude is expected to depend on the electron doping and tungsten mean valence, the similar W-shifts in all members are uniformly explained by a simple Bond Valence (BV) model. Here, the short and strongly covalent P-O bonds engage nearly 66% of the BVS of the bridging P-O-W oxygen atoms. Then tungsten is pushed asides cooperatively towards the center of the layers, and so in an antiferroelectric manner for symmetry reasons.

High-resolution low-temperature XRPD (Cu-$K_{\alpha 1}$ radiation) for *m* = 2 reveals a negative thermal expansion within the *ab* plane of α_{ab} = -5.6 10^{-6} K^{-1}, in contrast to the *m* = 4 compound. This behavior is illustrated in Fig. 3a by the opposite thermal evolution of the (0 0 3) and (4 -2 0) reflections peaks (see Fig. S2 in the supporting Information for details). Importantly, we already reported that the L-MPTB members at *m* = 3, 4 and 5 differ from their parent tungsten bronzes by their robust structural stability against commonly observed (in)commensurate modulations along with CDW-instabilities. Searching for such a behavior by diffraction for *m* = 2 also failed. Besides the “smooth” evolution of the lattice parameters on cooling (stabilized below 50 K), the imaging of the reciprocal space by single crystal XRD (300 K) and by electron-diffraction (293 K < T < 103 K) did not reveal the occurrence of any supercell spots nor diffuse scattering, thus validating a locked-trigonality see Fig. 3b, 3c and 3d. This structural rigidity is incompatible with the expected in-plane W-shifts occurring in CDW-processes, in accordance with the transport properties discussed below.

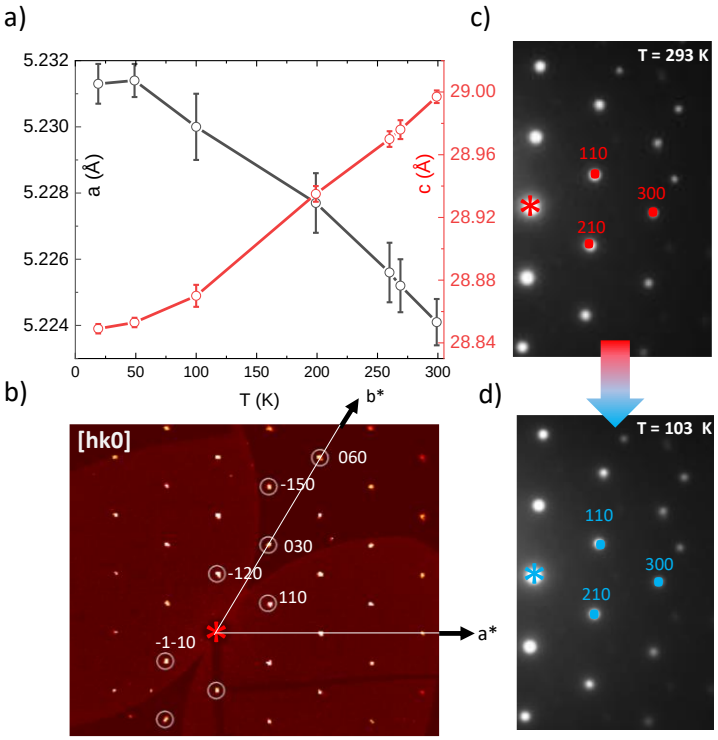

***Figure 3**. a) Lattice parameters a and c as a function of temperature. Negative thermal expansion is observed for a. $[Ba(PO_4)_2]W_2O_3$ (m = 2) diffraction data. b) hk0 reconstructed precession frame from SC-XRD. [001] zone axis electron-diffraction patterns at c) 297K and d) 103K.*

Physical properties. Next, we investigate resistivity, thermopower and specific heat of $Ba(PO_4)_2W_2O_3$ as a function of temperature. The results are compared with those measured for the other members of the L-MPTB series in Fig. 4.

The measured resistivity confirms the metallic behavior in *m* = 2, consistent with the other members across the series (see inset of Fig. 4a). Also in accordance with the rest of the series, there is no evidence for the existence of CDW instabilities. The various residual resistivities, however, reveal differences associated with the amount of defects that are present in the samples. Contrary to the other members, the measured Seebeck coefficient (S) for *m* = 2 is positive and increases with temperature (see Fig. 4b). On this figure, the experimental S(T) plots were fitted using a charge carrier thermo-diffusion term (which dominates the high-temperature behaviour) and a phonon-drag contribution [5,11], with results given in Table S5 and details of the fit are provided in section V (see the supporting Information). The reversed thermopower signs an increased importance of the phosphate spacer, as we will discuss below. Further, due to the metallic character of these systems, the corresponding specific heat contains both electronic and lattice contributions without any low-temperature anomaly. After subtraction of the lattice contributions fitted similarly to the previous members [5], the deduced Sommerfeld coefficient associated with the electronic contribution is plotted in Fig. 4d as a function of *m* and summarized in Table S5 and details of the fit is provided in section V (see Supporting Information for details). As a result, the concentration of charge electronic carriers

(2/*m* per W atom) decreases as *m* increases, logically being inversely related to the formal oxidation state of tungsten which is given by (4+(*m*−1)*6)/*m*. The remaining specific heat due to the lattice is shown in Fig. 4c as a function of temperature. A closer look at the low-temperature specific-heat data reveals a quasi-linear-in-T behavior together with a broad peak in the $C_p(T)/T^3$ plots (see inset in Fig. 3c). These features appear systematically across the entire series, including the new *m* = 2 compound. In the latter case, the bump is a little bit broader and shifted towards higher temperatures. These bumps are generally associated with phason-excitations (*i.e.* structural excitations) that emerge in the presence of aperiodic modulations as in the case of charge-density-wave orders (see *e.g.* [12,13]). The observation of these features in the L-MPTB systems, however, is surprising because their crystal and electronic structure both remain exceptionally stable (in particular, with no evidence of CDW order). All together these features suggest exotic electronic states at the frontier between emergent orders and unstable 2D-metals.

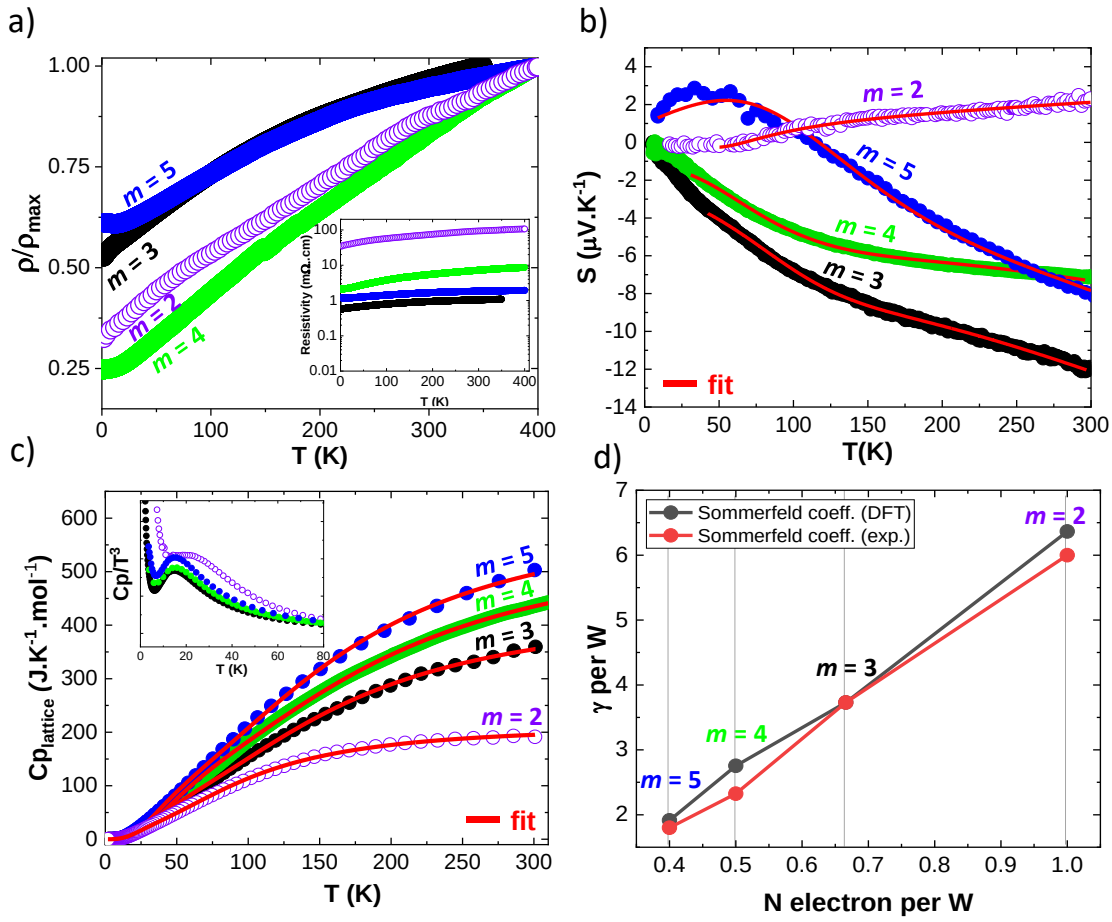

Figure 4. *Physical properties the L-MPTB series* $[Ba(PO_4)_2]W_mO_{3m-3}$. *Resistivity as a function of temperature (the inset shows the same data normalized to the resistivity at 300K) (a). Seebeck coefficient as a function of temperature (b). The solid line represents the fitted using the formula described in the supplementary section according to* [11]. *Lattice contribution to the specific heat as a function of temperature (the inset shows the same data at low temperature in a* C_p/T^3 *vs T plot, which should be constant according to the universal Debye law) (c). Experimental and calculated Sommerfeld coefficient of the electronic contribution to the specific heat obtained for the different members of the series (d).*

Electronic Structure. Formally according to the modular $[Ba(PO_4)_2][W_mO_{3m-3}]$ L-MPTBs picture, the spacers are electron-donors via their electropositive P and Ba atoms, leaving electron-doping withing the perovskite blocks as sketched in Fig. 1h. These later being built of corner-sharing WO_6 octahedra in the trigonal *ab* plane (see Fig. 1b), their electronic structure features zigzag chains of W-t_{2g} and O-π orbitals whose overlap can be expected to cause the observed metallicity metallicity (see Fig. S3 in the supporting Information for details)[14,15]. Specifically, there are intrachain t_{2g}-π-t_{2g} and interchain t_{2g}-t_{2g} δ weak overlaps that should yield six bands (three bands for each W atom in the unit cell from the aforementioned atomic-orbital overlaps). These bands belong to a well-separated manifold of W-t_{2g} derived states composed of a total of 3*m* bands dispersing along the *a*, *b*, and (*a* + *b*) directions only and hence with 1D character [16,17]. For *m* = 2, these states are formally occupied by 2 electrons so that the nominal filling of these bands is 1/3 each.

Fig. 5a shows the calculated band structure of the new *m* = 2 member of the L-MPTB series (see Supporting Information for the computational details and the comparison with the other members of the series in Fig. S4). We find three bands crossing the Fermi level, which is in agreement with the measured metallic character of these systems. The corresponding Fermi surface is illustrated in the inset of Fig. 5a (Fig. 5b). It shows a remarkable 2D character and, according to above, it can be regarded as the result of three sets of parallel planes forming quasi-1D nested surfaces. This suggests a "latent" tendency towards charge-density-wave order. This tendency, however, is visibly avoided in the L-MPTB systems most likely because of the rigidity provided by the barium phosphate spacer.

The calculated Fermi surface is associated with the well-separated W-t_{2g} manifold of derived states composed of a total of 3*m* bands. It is triply degenerate at the the Γ point for regular octahedra. For *m*=2, the degeneracy is broken into a low-lying singlet a_{1g} and upper doubly-degenerate e'_g levels denominated as (a_{1g} _ e'_g) hereafter. With respect to the crystal symmetry, this split is essentially due to the WO_6 trigonal distortion, which combines the W-off centering into two sets of W-O bond distances, and the octahedral elongation along the *c* axis deduced from the compared "*in-plane"* and "*along-c"* O-O distances. They have antagonist effects since the former and later are associated with (a_{1g} _ e'_g) versus (e'_g _ a_{1g}) splits respectively, from crystal field considerations. [18] Interestingly, a closer look at this splitting across the L-MPTB series reveals a progressive inversion of the relative position of the single a_{1g} and double degenerate e'_g bands (see Fig. S4 in the supporting Information). This happens whenever all the involved octahedra (from *m* = 2 to 5) show trigonal elongations along the *c* axis. This highlights a reversal of the crystal-field splitting of the initial W-t_{2g} states. For *m* = 5, the *elongated-like* (e'_g _ a_{1g}) split prevails, similarly to the $K(MoO_4)_2Mo_4O_9$ bronze case.[19] This reversal and the underlying trigonal distortion of the WO_6 octahedra immediately linked to the increased influence of the phosphate groups becoming more pronounced as *m* decreases, *i.e.* as the ratio of WO_6 in the

proximity to the spacer through W-O-P bridges, and the induced W shift becomes more and more prominent (see also the discussion).

Fig. 5c compares the total density of states (DOS) and the DOS contribution from the different W atoms computed for the L-MPTB series. The corresponding Sommerfeld coefficient is compared with its experimental value in Fig. 4d. The calculation captures the experimental trend with a quantitative agreement also. Moreover, from the corresponding band fillings (see below), we observe that the metallicity of these systems is mainly associated with the most central W atoms within the WO_3 slab, thus reinforcing its 2D character. This aspect is discussed below in relation to the oxidation state of the W atoms and their anti-polar displacement.

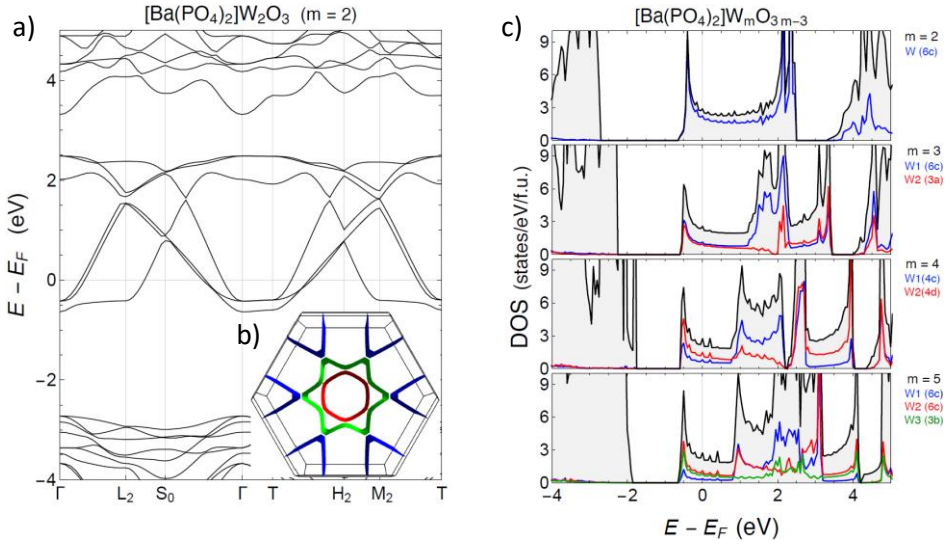

Figure 5. *Calculated electronic structure. a) Band structure and Fermi surface of $[Ba(PO_4)_2]W_2O_3$. This system displays well separated a manifold of six W-t_{2g} derived bands, with three of them crossing the Fermi level (see Fig. S4 for a comparison with the rest of the members of the L-MPTB series). b) The corresponding Fermi surface has a remarkable 2D character, and can be regarded as composed of three pairs of nested parallel planes (i.e. the superposition of 1D Fermi surfaces indicated by the gray lines). c) Total (black curves) and W-5d projected density of states (DOS), with the different Ws labelled according to their Wyckoff positions.*

DISCUSSION

W valence. We first discuss the uncommon pentavalent tungsten state in $[Ba(PO_4)_2]W_2O_3$ and the evolution of the metal valence across the L-MPTB series. To this purpose, we start by plotting the height along the c-axis of the different WO_6 octahedra and their average as a function of the nominal W valence of each compound including the d^0 case of the cubic WO_3 ($m\rightarrow\infty$) variant stabilized by doping. [20] The average height (see Fig. 6a and Table S4 in the supporting Information) decreases nearly linearly in agreement with the increase of the W ionic radius (IR) upon reduction (IR W^{6+} = 0.60Å and IR W^{5+} = 0.51Å [21]). The rather homogeneous distribution of octahedral size in each compound refutes any obvious W^{5+}/W^{6+} charge ordering tendency in all terms of our L-MPTB series. In contrast, the

variable W off-centering in each O_6 octahedron across the series may reflect differently such disproportionation.

In order to clarify this point, we inspect the filling of the W-t_{2g} derived bands from the computed electronic structure of these systems. Fig. 6b shows this quantity per W as a function of the nominal number of electrons per W across the L-MPTB series. For m = 2, the filling obtained from the total DOS is in tune with the nominal W^{5+}-d^1 configuration expected in this case. However, when filling is calculated from the W-derived states only, it turns out to be noticeably below its nominal value. The difference is due to the hybridization with O-p derived states. This difference decreases as m increases, which suggests that the W-O hybridization is higher in the proximity of the spacer (where, in addition, the W off-centering is more pronounced). In any case, the computed filling reveals a trend from the W^{5+}-d^1 configuration for m = 2 towards the W^{6+}-d^0 one of the WO_3 perovskite-type layers as m increases (see Fig. 6b).

Further, for m > 2, we find that the filling of the states associated with the outer tungsten atoms (W1) is always below the average filling while filling of the central Ws (W2 and W3) is significantly above that average (see Fig. 6b). As m increases, the outer W atoms (W1 and then W2 also) contribute less and less to the metallic behaviour which is eventually dominated by the Ws at the center of the WO_3 slab (i.e. W3 for m = 5). Therefore, the metallicity of these systems remains remarkably 2D even if the crystal structure tends to the bulk WO_3 on increasing m.

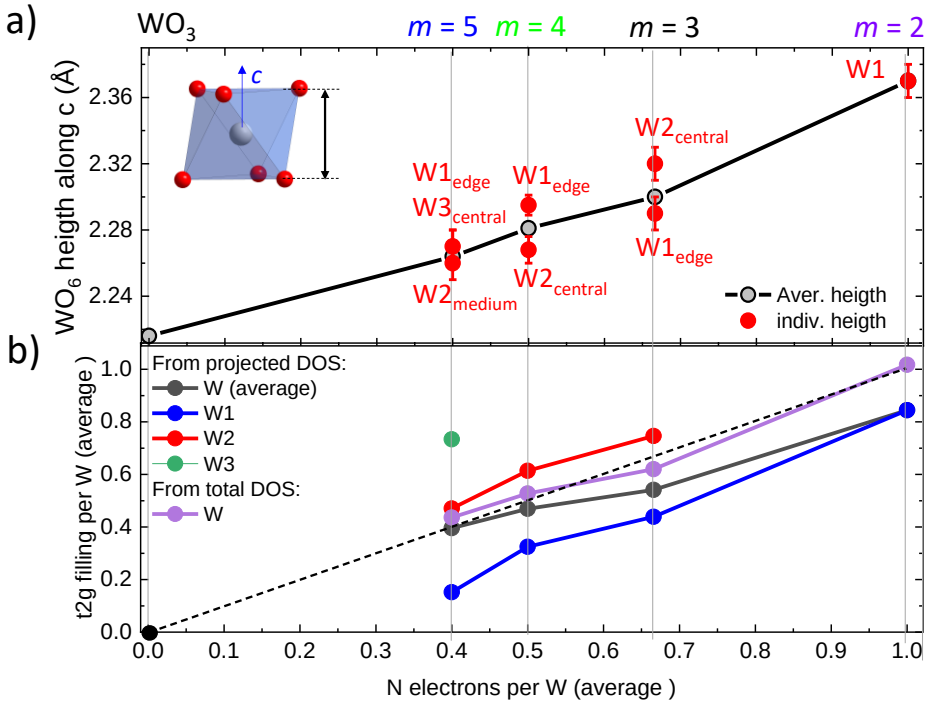

Figure 6. *a) Height of the different WO_6 octahedra along the c-axis as a function of the formal W valence across the entire L-MPTB series. The arbitrary offset of this plot is fixed with the m = 2 compound. b) Filling of the t_{2g} manifold per W atom computed from the total and W-projected DOS. The W atoms are labelled as in Fig. 1e-h, so that W1 always corresponds to the outer W of the WO_3 slab (i.e. the only ones for m = 2).*

Role of the spacer. Next, we discuss the relative importance of the phosphate spacer in the L-MPTB series $[Ba(PO_4)_2]W_mO_{3m-3}$ from the following observations. The new member at m = 2 displays negative thermal expansion within the trigonal *ab* plane (see Fig. 3a), which changes to positive across the series for m = 5 (see [5]). While the layered structure of the L-MPTBs justifies their anisotropic thermal, the distinct expansion properties behavior of the m = 2 phase could be related to that observed in other layered perovskites such as Sr_2IrO_4. [22] In that case, it has been associated with equatorial rotations of the IrO_6 octahedra in this tetragonal example. However, it is not allowed in the trigonal structure of the L-MPTBs. The behavior of m = 2 can then be regarded as reminiscent of the negative-thermal-expansion behavior of the prototype ReO_3 material [23]. In this case, the electron-phonon coupling is believed to play the key role, which can be expected to be different at the W-O-P bridges.

The Seebeck coefficient provides a direct measure of the electron-phonon coupling. This coefficient is positive for m = 2 and negative for the rest of the members of the L-MBTB series. However, the calculations show that the charge carriers have electron character in all these systems and are always related to the central Ws of the W_mO_{3m-3} blocks irrespective of m. Accordingly, we can assume that this Seebeck coefficient is the result of multiple couplings, and in the case of m = 2, it suggests a more direct effect of the spacer on the relevant electron-phonon interaction.

The increased influence of the $[Ba(PO_4)_2]$ spacers can also be deduced from the crystal-field splitting of the W-t_{2g} states across the series, as it was indicated above. In particular, we have shown that the band structure of the L-MPTB systems displays a progressive inversion of this splitting at the bottom of the W-t_{2g} manifold, suggesting a transition from the conventional (1e, 1a) configuration to the more exotic (*1a, 1e)* one as m decreases. This *virtual* trigonal compression like effect is assigned to the influence of the PO_4 ligand effect in the vicinity of the W ions, on the crystal field.

Anti-polar metallicity. The electronic disproportionation of the W atoms observed in the DFT calculations is the manifestation of the extraordinary effect that, even when the thickness of WO_3 slab increases, the metallicity is preserved in the L-MPTB series. This is rather counterintuitive since, as m increases, the nominal oxidation state of the W atom tends to 6+ and therefore should correspond to the d^0 configuration of bulk WO_3. Furthermore, the calculations reveal that such a metallicity has a 2D character since the conduction is due to the central W atoms of the WO_3 slab.

The different participation of the different W atoms in the overall conduction is, in part, certainly caused by the inductive effect of the PO_4 groups, as they polarize the electronic clouds along the W-O-P bridges. However, on closer inspection, we identify another superimposed mechanism that is crucial for the 2D character of the observed metallicity. Specifically, we notice that the off centering of the W atoms within the WO_6 octahedra is such that the W_mO_{3m-3} slab is composed of two polar sub-slabs

arranged in an anti-parallel fashion so that it contains a domain wall at the middle as illustrated in Fig. 1e-h. In fact, the hypothetical cubic phase of WO_3 is inherently soft with respect to polar displacements of this type [24-25] (although they are eventually preempted by structural distortions that increase the size of the unit cell in that case). Then, in the L-MPTB systems, it is natural to expect that the vicinity of the covalent P-O bonds induces the displacement of the W atoms according to the BV model afore proposed. These displacements cooperatively take place towards the center of the W_mO_{3m-3} slabs. In a purely ionic picture, the resulting anti-polar distortion of the WO_3 slab generate bound charges at the domain wall that would compensate the electron-donation of the spacers, see Fig. 1h. In reality, there is always an additional screening provided by the distortion the electronic clouds which then can be expected to lead to an increase in the carrier concentration at the center of the perovskite blocks. This is confirmed in our calculations. Thus, the central part of WO_3 block in the L-MPTB systems becomes analogous to the charged domain walls with enhanced conductivity that are observed in some ferroelectrics (see *e.g.* [26]).

CONCLUSIONS

$[Ba(PO_4)_2]W_2O_3$ was synthesized using a solid-state reaction method. Contrary to the related MPTBp compounds which exhibit 1D zigzag chains of $W^{5+}O_6$ octahedra, it shows a double-octahedral A-site empty perovskite layers and belongs to the newly discovered $[Ba(PO_4)_2]W_mO_{3m-3}$ L-MPTB family of compounds with m = 2. Although there is an evolution from the nominal 5+ (m = 2) towards 6+ for higher m values, with a clear insulating WO_3 bulk limit, the metallic behaviour in the series remains, confined in 2D octahedral layers with atomic thickness. In addition the analysis of the m = 2 member further validates the absence of the expected CDW-like instabilities in the entire series and the role of the $[Ba(PO_4)_2]$ spacer to lock-in rigid trigonal crystal structures incompatible with in-plane modulated W-shifts. Altogether, structural studies physical properties measurements and DFT calculations unravel this counterintuitive behavior and show that besides the influence of the phosphate spacers, the antipolar displacement of the tungsten atoms along with their concomitant induced polarity achieve the equivalent to charged domain walls in ferroelectrics. This effect genuinely increases the carrier concentration towards the centre of the WO_3 blocks and thus, preserves the 2D metallic character across the whole series. This sets the path for a novel design scheme to induce 2D metallic behaviour in layered oxides and related compounds.

MATERIALS AND METHODS

Routine purity verification was conducted using a Brucker D8 powder diffractometer, while single-crystal X-ray diffraction data were collected on a Bruker Quazar SMART APEXII instrument (see section

I in the supporting Information for details). Tracking the diffractogram temperature dependence down to low temperatures was performed on a High-resolution Rigaku SmartLabXE using monochromated X-rays (see section I in the supporting Information for details). Neutron powder diffraction (NPD) experiments were carried out on the D2B beamline of the ILL (Institute Laue Langevin, Grenoble, France) using λ = 1.59 Å in the range 0-155° at room temperature on grinded polycrystalline sample (see section I in the supporting Information for details). High-angle annular dark-field (HAADF) imaging was carried out using a TEM FEI TITAN Themis 300 (see section II in the supporting Information for details). DFT calculations were performed using the Quantum ESPRESSO package (see section IV in the supporting Information for details). Physical properties including Seebeck coefficient, resistivity, and heat capacity were measured on a Physical Properties Measurement System (PPMS) Dynacool-9T from Quantum Design (see section V in the supporting Information for details). Deposition numbers CCDC-2321390 contain the Supplementary crystallographic data for this paper. These data are provided free of charge by the joint Cambridge Crystallographic Data Centre and Fachinformations zentrum Karlsruhe Access Structures service.

ACKNOWLEDGEMENTS

We would like to express our sincere gratitude to C. Ritter from ILL and J. Wolber for their assistance with NPD measurements on the D2B beamline. Laurence Burylo at the UCCS is also acknowledged for her experimental contribution. HN thanks the Région Hauts de France for its financial support during his PhD. The Chevreul Institute (FR 2638), Region Hauts-de-France, and FEDER are acknowledged for funding the X-ray diffractometers and the PPMS magnetometer.

CONTENT OF THE SUPPLEMENTARY MATERIALS

It contains details on the Crystallographic refinement and parameters. Tables , figures and details of the fits of the electric , heat capacity and thermo-electric data. It also contains details on the 1st principle calaculations.

CONFLICT OF INTEREST

The authors declare no competing interests.

REFERENCES

(1) Dickens, P. G.; Whittingham, M. S. The Tungsten Bronzes and Related Compounds. *Q. Rev., Chem. Soc.* **1968**, *22* (1), 30. https://doi.org/10.1039/qr9682200030.

(2) Masetti, E.; Dini, D.; Decker, F. The Electrochromic Response of Tungsten Bronzes MxWO3 with Different Ions and Insertion Rates. *Solar Energy Materials and Solar Cells* **1995**, *39* (2), 301–307. https://doi.org/10.1016/0927-0248(95)00049-6.

(3) Zimmer, A.; Gilliot, M.; Tresse, M.; Broch, L.; Tillous, K. E.; Boulanger, C.; Stein, N.; Horwat, D. Coloration Mechanism of Electrochromic NaxWO3 Thin Films. *Opt. Lett.* **2019**, *44* (5), 1104–1107. https://doi.org/10.1364/OL.44.001104.

(4) Wöhler, F. XXXVIII. On Tungsten. *The Philosophical Magazine* **1825**. https://doi.org/10.1080/14786442508673961.

(5) Nimoh, H.; Arévalo-López, A. M.; Huvé, M.; Minaud, C.; Cano, A.; Glaum, R.; Mentré, O. Layered Monophosphate Tungsten Bronzes [Ba(PO4)2]WmO3m-3 : 2D Metals with Locked Charge-Density-Wave Instabilities. *Angew. Chem. Int. Ed. Engl.* **2023**, *62* (25), e202302049. https://doi.org/10.1002/anie.202302049.

(6) Roussel, P.; Pérez, O.; Labbé, P. Phosphate Tungsten Bronze Series: Crystallographic and Structural Properties of Low-Dimensional Conductors. *Acta. Cryst. B* **2001**, *57* (5), 603–632. https://doi.org/10.1107/S0108768101009685.

(7) *Physics and Chemistry of Low-Dimensional Inorganic Conductors*; Schlenker, C., Dumas, J., Greenblatt, M., Van Smaalen, S., Eds.; NATO ASI Series; Springer US: Boston, MA, 1996; Vol. 354. https://doi.org/10.1007/978-1-4613-1149-2.

(8) Duverger-Nédellec, E. Transitions Vers Des États Électroniques Complexes et Des Structures Super Périodiques Dans Les Bronzes Mono Phosphates de Tungstènes. These de doctorat, Normandie, 2017. https://www.theses.fr/2017NORMC239 (accessed 2024-03-06).

(9) Teweldemedhin, Z. S.; Ramanujachary, K. V.; Greenblatt, M. Magnetic and Electronic Transport Properties of the Monophosphate Tungsten Bronze (PO2)4(WO3)2m, *m* = 2. *J. Solid State Chem.* **1991**, *95* (1), 21–28. https://doi.org/10.1016/0022-4596(91)90372-O.

(10) Manthiram, A.; Goodenough, J. B. Lithium Insertion into Fe2(SO4)3 Frameworks. J. Power Sources Adv. **1989**, *26* (3), 403–408. https://doi.org/10.1016/0378-7753(89)80153-3.

(11) Kockert, M.; Mitdank, R.; Zykov, A.; Kowarik, S.; Fischer, S. F. Absolute Seebeck Coefficient of Thin Platinum Films. *J. Appl. Phys.* **2019**, *126* (10), 105106. https://doi.org/10.1063/1.5101028.

(12) a) Cano, A.; Levanyuk, A. P. Explanation of the Glasslike Anomaly in the Low-Temperature Specific Heat of Incommensurate Phases. *Phys. Rev. Lett. 93*, 245902. https://doi.org/10.1103/PhysRevLett.93.245902 b) G. Reményi, S. Sahling, K. Biljaković, D. Starešinić, J.-C. Lasjaunias, J. E. Lorenzo, P. Monceau, and A. Cano, Incommensurate Systems as Model Compounds for Disorder Revealing Low-Temperature Glasslike Behavior, Phys. Rev. Lett. 2015, 114, 195502. https://doi.org/10.1103/PhysRevLett.114.195502

(13) Wang, J.; Xiong, R.; Yin, D.; Li, C.; Tang, Z.; Wang, Q.; Shi, J.; Wang, Y.; Wen, H. Low-Temperature Specific Heat of the Quasi-Two-Dimensional Charge-Density Wave Compound KMo6O17. *Phys. Rev. B* **2006**, *73* (19), 193102. https://doi.org/10.1103/PhysRevB.73.193102.

(14) Canadell, E.; Whangbo, M. H. Conceptual Aspects of Structure-Property Correlations and Electronic Instabilities, with Applications to Low-Dimensional Transition-Metal Oxides. *Chem. Rev.* **1991**, *91* (5), 965–1034. https://doi.org/10.1021/cr00005a015.

(15) Canadell, E.; Whangbo, M. H.; Rachidi, I. E. I. Similarity of the Electronic Properties of the Monophosphate Tungsten Bronzes. *Inorg. Chem.* **1990**, *29* (19), 3871–3875. https://doi.org/10.1021/ic00344a043.

(16) Paul, S.; Ghosh, A.; Sato, T.; Sarma, D. D.; Takahashi, T.; Wang, E.; Greenblatt, M.; Raj, S. Electronic Band Structure and Fermi Surfaces of the Quasi–Two-Dimensional Monophosphate Tungsten Bronze, P4W12O44. *EPL* **2014**, *105* (4), 47003. https://doi.org/10.1209/0295-5075/105/47003.

(17) Whangbo, M.-H.; Canadell, E.; Foury, P.; Pouget, J.-P. Hidden Fermi Surface Nesting and Charge Density Wave Instability in Low-Dimensional Metals. *Science* **1991**, *252* (5002), 96–98. https://doi.org/10.1126/science.252.5002.96.

(18) Wang, Z.; Liu, L.; Zhao, M.; Zheng, H.; Yang, K.; Wang, C.; Yang, F.; Wu, H.; Gao, C. Identification of the Compressive Trigonal Crystal Field and Orbital Polarization in Strained Monolayer α-RuCl3 on Graphite. *Quantum Front.* **2022**, *1* (1), 16. https://doi.org/10.1007/s44214-022-00016-8.

(19) Whangbo, M. H.; Canadell, E.; Schlenker, C. Band Electronic Structure of the Purple Potassium Molybdenum Bronze K0.9Mo6O17. *J. Am. Chem. Soc.* **1987**, *109* (21), 6308–6313. https://doi.org/10.1021/ja00255a013.

(20) Palatnik, L. S.; Obol'yaninova, O. A.; Naboka, M. N.; Gladkikh, N. T. New Modifications of Tungsten Oxides. *Inorg. Mater. (USSR) (Engl. Transl.), v. 9, no. 5, pp. 718-720* **1973**.

(21) Shannon, R. D. Revised Effective Ionic Radii and Systematic Studies of Interatomic Distances in Halides and Chalcogenides. *Acta. Cryst. A* **1976**, *32* (5), 751–767. https://doi.org/10.1107/S0567739476001551.

(22) Sharma, P.; Singh, S.; Kuga, K.; Takeuchi, T.; Bindu, R. Synthesis and Structural Link to the Electronic and Magneto-Transport Properties of Spin–Orbit Mott Insulator Sr2IrO4. *J. Phys.: Condens. Matter* **2022**, *34* (43), 435402. https://doi.org/10.1088/1361-648X/ac8961.

(23) Liu, Y.; Wang, Z.; Wu, M.; Sun, Q.; Chao, M.; Jia, Y. Negative Thermal Expansion in Isostructural Cubic ReO3 and ScF3: Comput. Mater. Sci **2015**, *107*, 157–162. https://doi.org/10.1016/j.commatsci.2015.05.019.

(24) Hamdi H, Salje E K H, Ghosez P and Bousquet E 2016 First-principles reinvestigation of bulk WO3 *Phys. Rev. B* **94** 245124, https://doi.org/10.1103/PhysRevB.94.245124

(25) N. Mascello , N.A. Spaldin , A. Narayan, and Q.N. Meier , Theoretical investigation of twin boundaries in WO3 : Structure, properties,and implications for superconductivity, Phys. Rev. Research 2, 033460 (2020), https://doi.org/10.1103/PhysRevResearch.2.033460

(26) Meier D, Seidel J, Cano A, Delaney K, Kumagai Y, Mostovoy M, Spaldin N A, Ramesh R and Fiebig M 2012 Anisotropic conductance at improper ferroelectric domain walls *Nat. Mater.* **11** 284–8, DOI: 10.1038/nmat3249

For Table of Content Only